Korean J. Chem. Eng., 35(9), 1932-1940 (2018)
DOI: 10.1007/s11814-018-0084-y

pISSN: 0256-1115
eISSN: 1975-7220

Hydrothermal stability of different zeolites in supercritical water: Implication for synthesis of supported catalysts by supercritical water impregnation

Yuechao Zhang, Yingjie Li, Junjie Gu, Senlin Tian†, and Ping Ning

Faculty of Environmental Science and Engineering, Kunming University of Science and Technology, Kunming, Yunnan 650500, China
(*Received 5 March 2018 • accepted 11 May 2018*)

Abstract−Supercritical water (SCW) impregnation is an efficient and feasible method that has been used to prepare highly dispersed supported catalysts, but few studies have investigated the stability of support materials in supercritical water. Thus, our aim was to investigate the hydrothermal stability of zeolite supports (ZSM-5, TS-1, ZSM-35, HY, 13X, Beta, SAPO-11 and SAPO-34) as model compounds in supercritical water. Results showed that almost all of zeolites suffered from crystallinity change, structural properties degradation, obvious desilication and dealumination. The decrease of surface areas and the collapse of crystalline structures in HY, 13X, Beta, SAPO-11 and SAPO-34 were more serious compared to ZSM-5, ZSM-35 and TS-1. The micropore areas and acidity of all SCW-treated zeolites were reduced. 13X with lower Si/Al ratio had higher hydrothermal stability than HY due to the formation of extra-framework Al (EFAL). EFAl also generated strong Lewis acid sites determined by ammonia temperature-programmed desorption and ^{27}Al magic angle spinning nuclear magnetic resonance. Desilication and dealumination were simultaneous, and led to the increase of framework Si/Al ratio. ZSM zeolites (ZSM-5, ZSM-35 and TS-1) had higher hydrothermal stability than HY, 13X, Beta, SAPO-11 and SAPO-34 in SCW.

Keywords: Supercritical Water Impregnation, Supported Catalysts, Hydrothermal Stability, Zeolite Supports

INTRODUCTION

Supercritical water (SCW) has received considerable attention recently as a new chemical reaction field for synthesizing catalysts of metal oxide particles [1-3]. Various kinds of nanoparticle preparation techniques have been developed based on supercritical water as a preparation method [1,4-10]. Among them, supercritical water impregnation (SCWI) is generally acknowledged as a method for preparing supported catalysts [10-16]. By utilizing the high diffusivity of supercritical water, SCWI method allows nanoparticles to deposit on support surfaces as well as inside the pores in highly dispersed conditions.

According to previous studies, many reports have deposited nanoparticles into porous materials enhanced by gas-like transporting properties of SCW to obtain catalysts with high performance. For example, Otsu and Oshima exploited the reactive properties of SCW to deposit nanoparticles of several metals in the pores of porous materials [10-12]. Zhao et al. reported the improvement of dispersity in CeO_2 nanoparticle deposition onto multiwall carbon nanotubes when the catalysts were prepared with SCW [13]. Xu and Teja deposited α-Fe_2O_3 nanoparticles on activated carbon and obtained egg-shell and uniform dispersions by the SCWI method [14]. Qiu et al. prepared a series of catalysts by depositing metal oxide particles onto the activated carbon using the SCWI method for the removal of H_2S from hot coal gas [15,16]. As stated above, the SCWI method in preparing catalysts is a promising method, which not only can make particles have a uniform size and stabilizing chemical composition, but also uses the water as a reaction medium, avoiding the use of toxic solvents and simplifying the process and post-treatments.

However, in the SCW system, water molecules are highly reactive in interacting with material surfaces, including catalyst supports, thus altering surface physicochemical properties and causing severe corrosion or decomposition of these materials. To date, very limited information has been available for the structure alterations of catalyst supports in SCW system. Many studies have primarily focused on the degradation characteristics of target contaminants with supported catalysts in SCW conditions, such as CuO/ZSM-5 [17,18], CuO/ZSM-48 [17,19], CuO/HY [17], ZSM-5 [20,21], Beta [20,21], HY [20,21], SAPO-11 [21], MCM-41 [21], MoO_3/Al_2O_3 [22], CeO_2/Al_2O_3 [23], La_2O_3/Al_2O_3 [23], MgO/Al_2O_3 [23], Pt/Al_2O_3 [24], Ru/Al_2O_3 [24], WO_3/TiO_2 [25], Pt/TiO_2 [26], yet few studies have investigated the hydrothermal stability of these catalyst supports. However, for carbon materials, there are some reports referring to the physicochemical property changes under SCW conditions. Ashraf and Dastgheib reported the interactions of SCW with a series of carbon materials (e.g., graphite plate, highly ordered pyrolytic graphite, porous graphite sample, diamond-coated stainless steel sample) under oxic or anoxic conditions [27]. Matsumura and Xu studied the gasification characteristics of a granular coconut-shell activated carbon in SCW (600-650 °C, 25.5-34.5 MPa) [28]. Sanchez and Salvador utilized SCW activation to regenerate phenol-saturated activated carbon, leading to increases in the values of the specific surface area and the point of zero charge [29]. Nevertheless,

†To whom correspondence should be addressed.
E-mail: tiansenlin@outlook.com

there are a huge number of other materials applied for catalyst supports (e.g., zeolites, Al_2O_3, TiO_2), so it is necessary to systematically study the physicochemical property changes and hydrothermal stability of supports for making catalysts with superior activity and favorable stability using SCWI.

Hence, it was of interest to investigate the physicochemical property changes and hydrothermal stability of eight microporous zeolites (TS-1, ZSM-5, ZSM-35, 13X, Y, Beta, SAPO-11 and SAPO-34) as model compounds in SCW at 385 °C, 22.5±0.2 MPa and 10 min. The changes of physicochemical properties in zeolites, which could act as an instrument for stability evaluation, were observed by X-ray diffraction, inductively coupled plasma-optical emission spectrometer, N_2 adsorption-desorption, ammonia temperature-programmed desorption, Fourier transform infrared spectroscopy, ^{27}Al and ^{29}Si magic angle spinning nuclear magnetic resonance characterizations. Physicochemical properties included crystalline structure, pore structure, Si/Al ratio, acid site distribution and acid content.

MATERIALS AND METHODS

1. Materials

ZSM-5 (SiO_2/Al_2O_3=25), HY (SiO_2/Al_2O_3=3.5) and SAPO-11 ($SiO_2/P_2O_5/Al_2O_3$=0.7 : 1 : 1) were purchased from the Catalyst Plant of Nankai University. SAPO-34 ($SiO_2/P_2O_5/Al_2O_3$=0.4 : 1 : 1), ZSM-35 (SiO_2/Al_2O_3=40) and TS-1 (SiO_2/TiO_2=75) were obtained from Shanghai Zhuoyue Chemical Technology Co., Ltd. Beta (SiO_2/Al_2O_3=40) was purchased from Nanjing Jicang Nano Technology Co., Ltd. 13X (SiO_2/Al_2O_3=2.5) was acquired from Sinopharm Chemical Reagent Co., Ltd. Ultrapure water was prepared in the laboratory by using an ultrapure water production system (Sichuan Wo Te Instruments Equipment Co., Ltd.).

2. Supercritical Water (SCW) Treatment Processes

The studied zeolites were washed by ultrapure water, and dried at 100 °C for 12 h prior to SCW experiments. A batch autoclave reactor with a backpressure regulator (upper pressure limit of 30 MPa) and a thermocouple temperature sensor (upper operating temperature of 700 °C) were used in the experiments. Experimental solutions were prepared by addition of zeolites and ultrapure water with a mass ratio of zeolite to water of 12.5. All experiments were involved using a batch autoclave reactor made of stainless steel (sus 316) having an inner volume of 150 mL.

The quantitative zeolite powders and ultrapure water were added to the autoclave, which was then heated at a constant rate until a final temperature was attained (the time for this heating step was about 115 min in most experiments). The autoclave was then maintained at the reaction temperature (about 385 °C) and reaction pressure (22.5±0.2 MPa) for a specified reaction time (about 10 min). Finally, the autoclave was cooled to room temperature in a cool water bath to stop the reaction. The resulting zeolites were isolated from the mixture by using a membrane filter, washed several times with ultrapure water and to remove residues, and then dried at 105 °C for 12 h in an oven.

3. Zeolite Characterization

The powder X-ray diffraction (XRD) analysis of parent zeolites and all SCW-treated samples was recorded on an Empyrean analytical diffractometer with Cu-Kα radiation (k=1.54 Å) using 45 KV tube voltage, and 40 mA tube current scan range was from 5 to 50 degree 2 - theta. X-ray powder patterns were used to calculate relative crystallinity (RC) of all the zeolites based on the intensity of the 5 strong characteristic peaks.

High-resolution transmission electron microscopy (HRTEM) images were obtained with a JEOL JEM-2100F instrument operating at 200 kV. Samples were suspended in ethanol with ultrasonic treatment and dropped on an ultra-thin porous carbon grid.

The bulk Si, Al, P and Ti of the zeolite samples were determined by inductively coupled plasma-optical emission spectrometer (ICP-OES; Optima model 7000DV, PerkinElmer, USA) after dissolution of the solids in the mixture of HNO_3/HF/HCl (1 : 1 : 3).

The N_2 adsorption-desorption measurements at 77 K were performed on a Micromeritics ASAP 3020 surface area analyzer (Micromeritics Instrument Corp., Norcross, GA). The BET surface area (S_{BET}) was obtained through the BET method. The micropore and mesopore distributions were determined by applying the t-plot and BJH theories, respectively. The BET particle diameter was calculated as d_{BET} derived from the formula $6/(S_{BET} \times \text{density})$ [30].

The acid properties of these zeolites were determined by ammonia temperature-programmed desorption (TPD), employing a Micromeritics AutoChem 2920 instrument with a thermal conductivity detector (TCD) using helium as carrier gas. The sample (100 mg) was pretreated at 450 °C in He (40 mL min^{-1}) for 1 h. After cooling to 100 °C, pure NH_3 (40 mL min^{-1}) was passed through the sample for 30 min. Subsequently, a flow of He (40 mL min^{-1}) was passed through the reactor during 60 min to remove weakly adsorbed ammonia on the zeolite. Desorption of NH_3 in the effluent He stream was measured in the range of 100-700 °C with a heating rate of 10 °C min^{-1}.

The characteristic vibration bands of the samples were analyzed by Fourier transform infrared spectroscopy (FTIR) (Thermo Scientific Nicolet iZ10 spectrometer, USA) at a resolution of 4 cm^{-1} in the range of 400-4,000 cm^{-1} with KBr pellet at a resolution of 4 cm^{-1}.

^{29}Si and ^{27}Al magic angle spinning nuclear magnetic resonance (MAS NMR) spectra were recorded on a Bruker AVIII-HD600 MHz solid-state NMR spectrometer using a ZrO_2 rotor. The ^{29}Si resonance frequency was 52.6 MHz and the spinning rate 10 kHz. Spectra were obtained after irradiation of the sample with 1.7 μs excitation pulse and 20 s relaxation delay. The ^{27}Al spectra were recorded at 79.5 MHz with a spinning rate of 14 kHz using 1.22 μs excitation pulse and 30 s relaxation delay. The MAS NMR Spectra were normalized to the same mass of sample.

RESULTS AND DISCUSSION

1. XRD Pattern of Zeolites

The X-ray patterns of parent and SCW-treated zeolites are shown in Fig. 1. The XRD patterns of SAPO-34, SAPO-11, Beta, HY (13X), ZSM-5 (TS-1) and ZSM-35 were consistent with the CHA, AEL, BEA, FAU, MFI and FER structures of these zeolites [31-34]. Compared to HY, 13X had the same framework type (FAU) and lower Si/Al ratio. TS-1 (titanium silicalite) and ZSM-5 (aluminosilicate) also had the same framework type (MFI). The hydrothermal stability of different crystalline structures in zeolites was distinctly different, as shown in Fig. 1. The crystalline structures of ZSM-35,

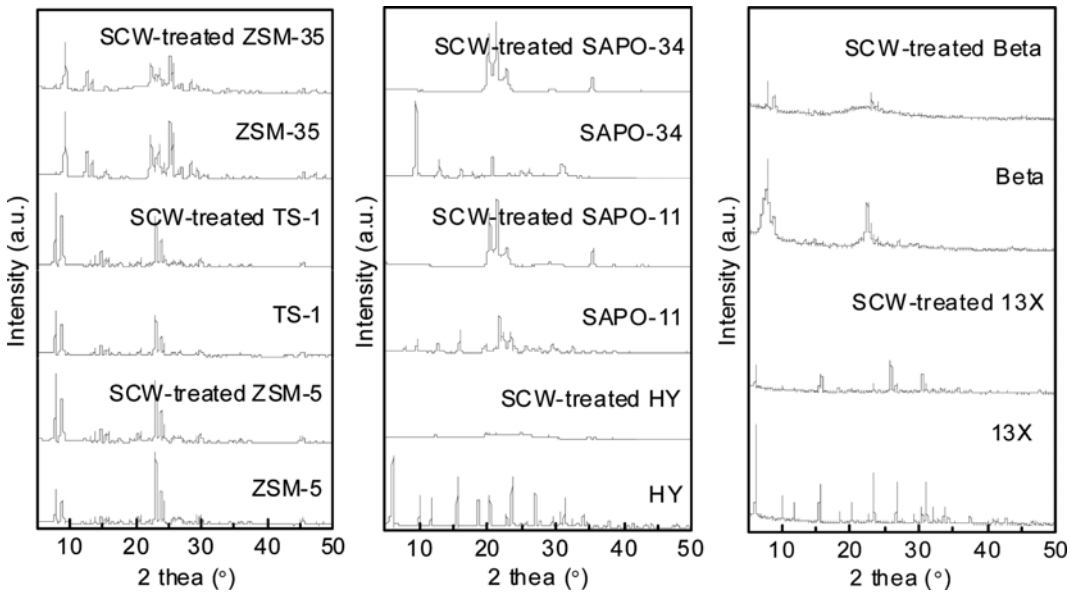

Fig. 1. XRD patterns of zeolites before and after SCW treatment at 22.5 MPa, 385 °C and 10 min.

Table 1. The effect of SCW treatment at 22.5 MPa, 385 °C and 10min on relative crystallinity and d_{BET} of zeolite

		ZSM-5	TS-1	ZSM-35	13X	HY	Beta	SAPO-11	SAPO-34
RC (%)	SCW-treated	100	100	100	100	--	--	--	--
	Parent	92	96	92	80	--	--	--	--
d_{BET} (nm)	SCW-treated	18.56	16.59	18.95	33.92	26.7	65.66	137.5	108.9
	Parent	16.44	16.52	15.87	9.75	1.7	10.61	32.67	9.89

ZSM-5 and TS-1 did not completely collapse after SCW treatment, and the characteristic diffraction peaks could be observed from Fig. 1. Relative crystallinity of the three SCW-treated zeolites increased as listed in Table 1. Nevertheless, the intensity of the XRD peaks of 13X and Beta after SCW treatment decreased significantly. According to FTIR data (Fig. 4), we could observe that 13X kept the band at 560 cm^{-1}, but the band of Beta at 575 cm^{-1} disappeared in the corresponding spectra. Due to the bands at 560 and 575 cm^{-1} assigned to the existence of double ring by tetrahedral SiO_4 and AlO_4 units, the results indicated that the crystalline structure of SCW-treated 13X was maintained to a certain extent, but the structure of Beta completely collapsed. As listed in Table 1, the crystallinity of SCW-treated 13X also increased. The following reasons for increasing the crystallinity of zeolites due to SCW treatment might be made:

(1) An increase in crystallinity could be due to the extraction of extra-framework aluminum from zeolites [35];

(2) An agglomeration of zeolites could explain an increase in crystallinity [36].

Because of the increase of d_{BET} after SCW treatment as shown in Table 1, a possible explanation for the increase of relative crystallinity can be attributed to the agglomeration of zeolites [36]. The agglomeration was also observed in the TEM images of parent and SCW-treated 13X in Fig. S1.

But the crystalline structures of SAPO-34, SAPO-11, Beta and HY completely collapsed in SCW. The new XRD peaks of SCW-treated SAPO zeolites (SAPO-34 and SAPO-11) could be attributed to a synthetic aluminum phosphate of the tridymite structure type [37]. The hydrothermal stability and relative crystallinity of Beta decreased with increase of temperature and steam pressure, especially when the value increased higher than 200 kPa [38]. As shown in Fig. 1, high temperature and high pressure in SCW led to the serious collapse of the crystalline structure in Beta. Generally speaking, Si/Al ratio of zeolites has a significant role in hydrothermal stability; lower Si/Al ratio could improve hydrothermal stability [39,40]. 13X had higher hydrothermal stability than HY. A possible explanation is that an increased stability upon incorporation of aluminum (extra-framework Al) near the surface of zeolites was found in SCW, aluminum atoms in this position were capable of protecting the framework against hydrolysis [39]. The effect of surface aluminum species on stability was much more than that of aluminum within the pore walls [39]. NH_3-TPD and ^{27}Al MAS NMR data (Fig. S2) verified the formed extra-framework Al (EFAL) after SCW treatment. In addition, as listed in Table 1, SCW-treated zeolites increased relative crystallinity, due to the crystalline structures in a state of incomplete collapse.

2. Structural Characteristics of Zeolites

As shown in Fig. S3, according to the IUPAC classification [41], N_2-adsorption-desorption isotherms of parent zeolites are of classic type I with H3 or H4 hysteresis loop contributed to slit-shaped pores [42,43]. The structural characteristics of parent and SCW-treated zeolites derived from the isotherms (Fig. S3) are listed in

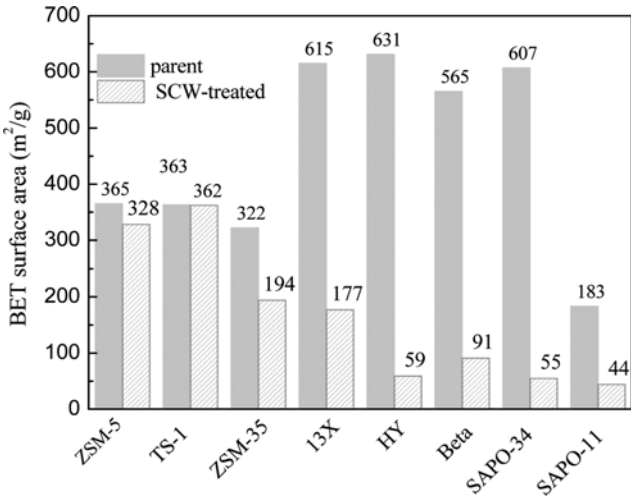

Fig. 2. BET surface area of parent and SCW-treated zeolites at 22.5 MPa, 385 °C and 10 min.

Table S1. The BET surface areas of SAPO-34, SAPO-11, beta, HY (13X), ZSM-5 (TS-1) and ZSM-35 before and after SCW treatment are shown in Fig. 2. The decreased percentage of surface area and pore volume in zeolites before and after SCW treatment is summarized in Table 2. The surface area and pore volume of all zeolites decreased. SCW-treated ZSM zeolites (TS-1, ZSM-5 and ZSM-35) with the lowest level of decreased percentage of BET surface area (0.003%, 10.1% and 39.8%, respectively) had higher hydrothermal stability than 13X, HY, Beta and SAPO zeolites. In addition, TS-1 had higher hydrothermal stability than ZSM-5. A possible explanation is that titanium atoms in tetrahedral positions had strong hydrophobic properties [32]. The decreased percentage of micropore surface area of TS-1, ZSM-5 and ZSM-35 was 5%, 17.5% and 46.0%, respectively.

After SCW treatment, the decreased percentages of BET and micropore surface area in 13X were smaller than those of HY, as listed in Table 2. 13X had higher hydrothermal stability than HY, which was in agreement with XRD data. As shown in Table S1, the values of external surface area in 13X, HY and ZSM zeolites increased after SCW treatment. High value of external surface area was advantageous in the regeneration process of catalytic cracking catalysts, because the removal of coke from the external surface was easier and less aggressive than the combustion of the internal one [44,45]. In addition, high external surface area implied a high proportion of external acid sites and might have high catalytic cracking activity [44,45].

The decreased percentage of micropore surface area of Beta was 86.9% (Table 2). A small amount of micropore structure still remained in Beta as well as HY. HY-generated H3 hysteresis loop contributed to slit-shaped pores, but the H4 hysteresis loop of Beta almost disappeared, as shown in Fig. S3. Moreover, ZSM-35 and 13X also generated obvious hysteresis loops H3 and H4. The decreased percentage of micropore surface area in SCW-treated SAPO zeolites was 100%, due to a synthetic aluminum phosphate of the tridymite structure type obtained from the XRD patterns. Based on the obtained results, it could be concluded that ZSM zeolites have higher hydrothermal stability than other zeolites. The hydrothermal stability of 13X with lower Si/Al ratio was higher than HY in SCW. The micropore structure of SAPO zeolites disappeared after SCW treatment due to the crystal-phase transformation.

3. NH_3-TPD Spectra of Zeolites

NH_3-TPD is a frequently used method for determining the acid strength distribution. NH_3-TPD profiles of parent and SCW-treated zeolites are shown in Fig. 3. In the temperature range of 100 to 700 °C, giving rise to three main peaks (L, M and H) at low (100-300 °C), moderate (300-500 °C) and high temperature (500-700 °C), respectively. The three peaks correspond to the weak, moderate and strong acid sites [46]. The L peak was attributed to the desorption of strongly physisorbed and chemisorbed NH_3 on external silanol groups. The M peak was due to NH_3 desorption from weak Brønsted (B) and Lewis (L) acid sites, while the H peak represented NH_3 desorption from strong Brönsted acid sites and Lewis acid sites [46].

There are two main peaks (L and M) in the profiles of the parent ZSM zeolites (TS-1, ZSM-5 and ZSM-35) in Fig. 3, and the distributions of acid sites were similar. The weak L acid sites of the M peak were assigned to unsaturated tetrahedrally coordinated titanium atoms, extra-framework Al species ($Al(OH)_2^+$ and $Al(OH)^{2+}$) and framework defects (coordinatively unsaturated framework Al atoms) [47,48]. In addition, a decrease of acid amount matched an

Table 2. The decrease of surface area and pore volume in zeolites before and after SCW treatment at 22.5 MPa, 385 °C and 10 min

	BET surface area (%)	Micropore surface area (%)	External surface area (%)	Total pore volume (%)	Micropore volume (%)	Mesopore volume (%)
ZSM-5	10.1	17.5	−42.2	−2.8	18.2	−108.0
TS-1	0.003	5.0	−35.7	−9.1	2.2	−24.6
ZSM-35	39.8	46.0	−45.4	17.6	46.5	−9.6
13X	71.2	84.2	−40.6	47.9	83.3	−18.1
HY	90.6	95.2	−50.0	26.0	98.2	−360.5
Beta	83.9	86.9	76.1	79.4	86.7	75.8
SAPO-34	90.1	100.0	−37.5	74.2	100.0	−11.8
SAPO-11	76.0	100.0	27.9	57.7	100.0	45.5

The decreased percentages of surface area and pore volume were calculated according to the following formula: (Surface area (parent)−Surface area (SCW-treated))/Surface are (parent); (Pore volume (parent)−Pore volume (SCW-treated))/Pore volume (parent)

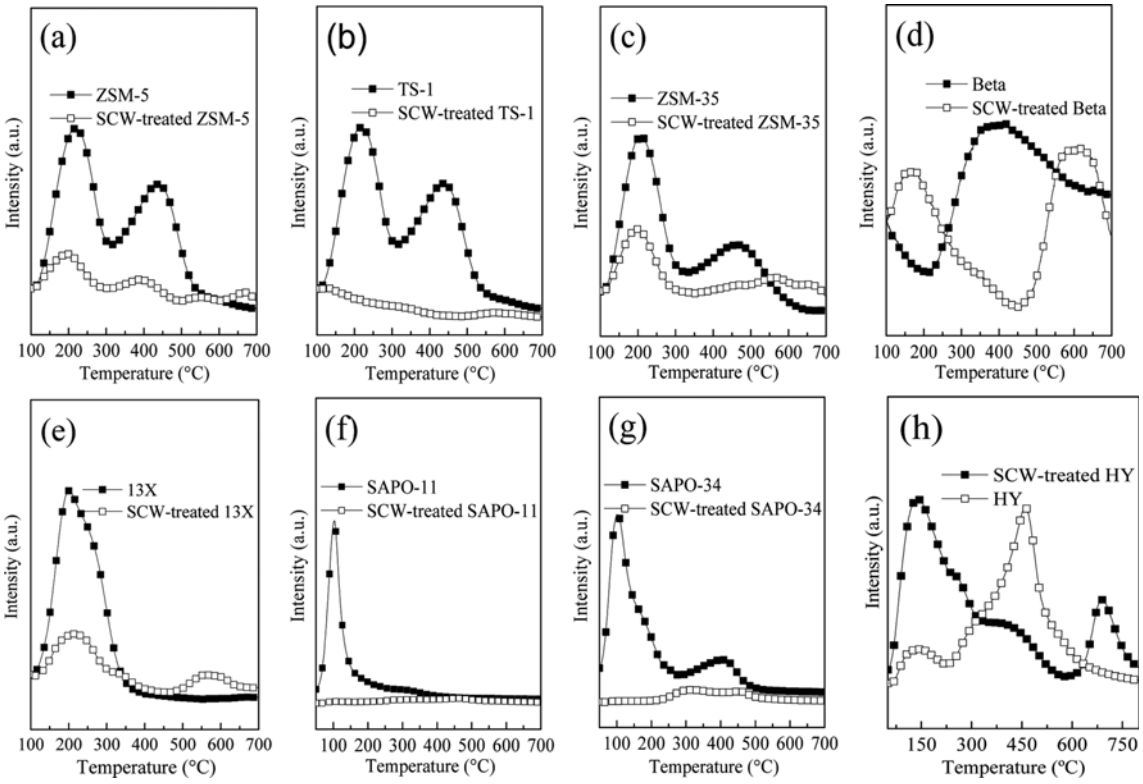

Fig. 3. NH_3-TPD profiles of zeolites before and after SCW treatment at 22.5 MPa, 385 °C and 10 min: (a), (b), (c), (d), (e), (f), (g) and (h) were ZSM-5, TS-1, ZSM-35, Beta, 13X, SAPO-11, SAPO-34 and HY zeolites, respectively.

Table 3. ICP-OES data of parent zeolites and zeolites treated by SCW at 22.5 MPa, 385 °C and 10 min

Sample		Molar ratio		Sample		Molar ratio	
		Si/Al[a]	Si/P[b]			Si/Al[a]	Si/P[b]
Parent	HY	5.40		SCW-treated	HY	5.18	
	ZSM-35	34.06			ZSM-35	30.44	
	ZSM-5	24.92			ZSM-5	20.00	
	TS-1	69.41[c]			TS-1	60.76[c]	
	SAPO-34	3.08	2.88		SAPO-34	1.92	1.80
	SAPO-11	0.50	0.46		SAPO-11	0.48	0.48
	13X	2.50			13X	2.26	
	Beta	22.02			Beta	20.18	

[a]$Si/Al=SiO_2/Al_2O_3$
[b]$Si/P=SiO_2/P_2O_5$
[c]SiO_2/TiO_2

increase of Si/Al ratio in zeolites [49]. Therefore, the obvious decrease of acid amount in the SCW-treated ZSM zeolites signified the decrease of Al and Ti (TS-1) content. According to ICP-OES data (Table 3), Si/T (Al or Ti) ratio of parent zeolites in the solid (framework and extra-framework) was higher than SCW-treated zeolites, indicating the increase of T relative content. But, according to NMR data, Si/Al ratio of SCW-treated zeolites in the framework was higher than parent zeolites. These results indicated that SCW treatment increased extra-framework (strong L acid sites=H peak) but decreased framework T (Al or Ti) contents.

In addition, a weak H peak in the profiles of the SCW-treated ZSM zeolites could be due to strong L acid sites derived from some extra-framework alumina species formed by dihydroxylation [48]. The dehydroxylation in the neighborhood of a lattice Al atoms was always accompanied by its release from the framework [48]. According to XRD data, the crystalline structure remained in 13X as well as the ZSM zeolites, and also exhibited a similar tendency that the acid amount of L peak decreased obviously and generated an obvious H peak, which could be assigned to strong L acid sites in the NH_3-TPD profiles.

The NH_3-TPD profiles (Fig. 3) of Beta, HY and SAPO zeolites (SAPO-34 and SAPO-11) before and after SCW treatment are

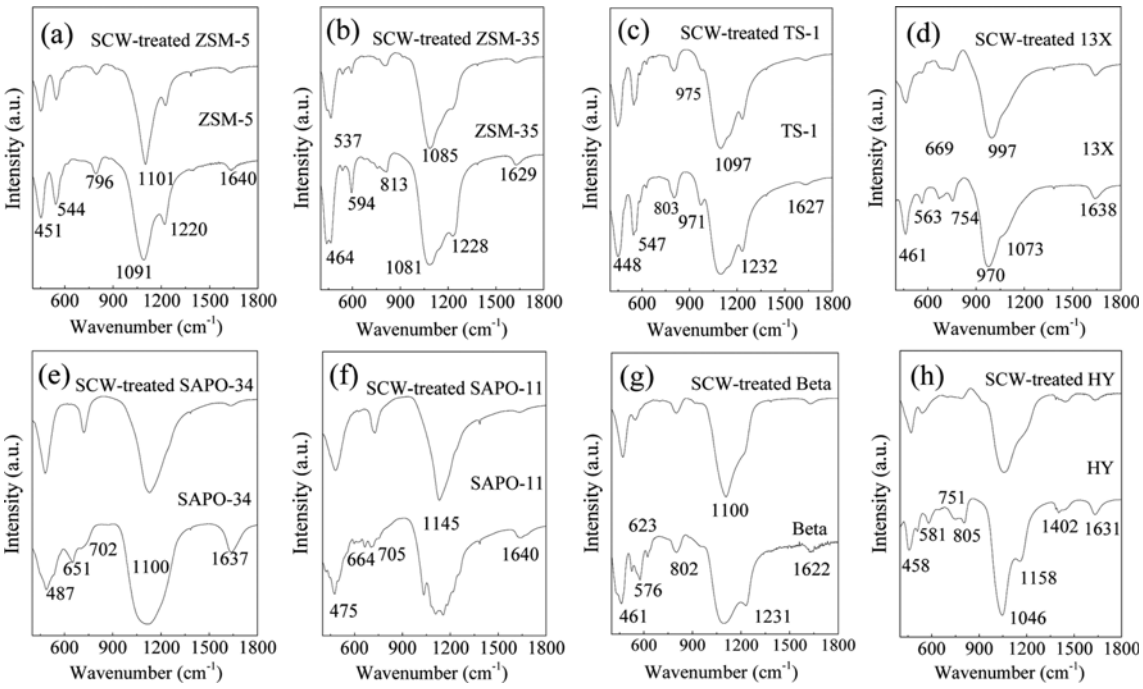

Fig. 4. FTIR spectra of zeolites before and after SCW treatment at 22.5 MPa, 385 °C and 10 min: (a), (b), (c), (d), (e), (f), (g) and (h) were ZSM-5, TS-1, ZSM-35, Beta, 13X, SAPO-11, SAPO-34 and HY zeolites, respectively.

shown in Fig. 3. After SCW treatment, Beta and HY remained a small amount of micropores similar to 13X and ZSM zeolites, and also generated an obvious H peak. But SCW-treated SAPO zeolites did not generate a new H peak and had no the micropore structure due to the complete collapse of the crystalline structure after the phase transformation (Fig. 1). The possible explanation for these observations is that SCW treatment resulted in the appearance of an H peak (strong L acid sites) due to the remaining micropore structure in SCW-treated zeolites.

4. FTIR Spectra of Zeolites

FTIR results of parent and SCW-treated zeolites are shown in Fig. 4. The bands in the spectrum around 400-500 cm^{-1} are due to the T-O bending vibrations of the SiO_4 and AlO_4 internal tetrahedral [50-53]. The bands at 500-650 cm^{-1} are assigned to structure-sensitive vibrations of double rings in the framework of zeolites. The adsorption signals between 1,000 and 1,200 cm^{-1} are attributed to the asymmetric stretch of Si-O-T linkage (where T=Si, Al and P). The bands of parent and SCW-treated 13X at 970 and 997 cm^{-1} also were due to the asymmetric stretch of Si-O-T linkage (where T=Si and Al). Bands in the lattice region of 400-1,300 cm^{-1} are mostly the vibration bands in the framework of zeolites. The bands around 1,602 cm^{-1} are assigned to deformational vibrations of adsorbed water molecules [52].

The peaks of SCW-treated 13X and ZSM zeolites at 500-650 cm^{-1} could be observed, which were attributed to the existence of double rings (crystalline structural characteristics). The decrease of the peak intensity in SCW-treated 13X and ZSM-35 was more serious than that of ZSM-5 and TS-1, which was in agreement with BET data (Table 2). The peaks at 1,091 cm^{-1} (ZSM-5), 1,081 cm^{-1} (ZSM-35) and 970 cm^{-1} (13X) were observed to shift towards higher wavenumbers with increasing Si/Al ratio of the three zeolites (aluminum silicate) [50]. This shift is due to the slightly lower mass of Al as compared to that of Si [50]. The bands at 1220 (ZSM-5) and 1232 (TS-1) cm^{-1} not only specified the existence of pores with 3D channel [51], but also the bands around 450, 545 and 800 cm^{-1} indicated the crystalline structure of ZSM-5 and TS-1. The bands at 400-900 cm^{-1} were assigned to the crystalline structure of SCW-treated ZSM-35 and 13X. As shown in Fig. 4, FTIR spectra specified that 13X and ZSM zeolites maintained their crystalline structure in different degrees after SCW treatment, which was consistent with XRD and BET data.

The band at 971 cm^{-1} (TS-1) was associated with the stretching Si-O vibrational mode perturbed by a polymeric structure formed by [SiO_4] and [TiO_4] units [54]. The decrease in the adsorption peak strength was observed in Fig. 4 due to the decrease of Ti content in SCW-treated TS-1. The bands around 651, 664, 525 and 510 cm^{-1} signified the existence of double ring structures in parent SAPO-34, SAPO-11, Beta and HY, but disappeared after SCW treatment. According to XRD and FTIR results, the crystalline structures of the SCW-treated zeolites collapsed (TS-1, ZSM-5, ZSM-35 and 13X) and even disappeared (SAPO-34, SAPO-11, Beta and HY), and SCW treatment increased Si/Al ratio of ZSM-5, ZSM-35 and 13X.

5. ^{29}Si and ^{27}Al MAS NMR Spectra of Zeolites

For revealing the transformation of Si and Al in zeolites after SCW treatment, the ^{29}Si and ^{27}Al NMR MAS spectra of parent and SCW-treated ZSM-5 as a representative zeolite are shown in Fig. 5. In the ^{29}Si NMR MAS spectra, the resonances around −112 ppm, −106 ppm, −102 ppm, and −91 ppm were assigned to Si(4Si, 0Al), Si(3Si, 1Al), Si(3Si, 0Al) and Si(1Si, 3Al) corresponding to Q^4(0Al),

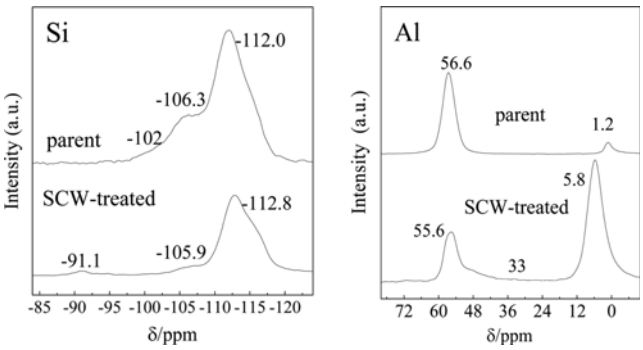

Fig. 5. ^{29}Si and ^{27}Al MAS NMR spectra of parent and SCW-treated ZSM-5 at 22.5 MPa, 385 °C and 10 min.

Table 4. ^{29}Si and ^{27}Al MAS NMR spectra of ZSM-5 before and after SCW treatment at 22.5 MPa, 385 °C and 10 min

	ZSM-5	SCW-treated ZSM-5
Framework Si/Al ratio[a]	19.1	30.3
Bulk Si/Al ratio	24.9	20.0
Intensity (%)[b]		
Si(4Si, 0Al)	78.7	92.9
Si(3Si, 1Al)	21.3	4.1
Si(1Si, 3Al)		3.0
Intensity (%)[c]		
Tetrahedral Al	78.1	28.9
Octahedral Al	21.9	71.1

[a]Calculated using the formula in [56]
[b]Obtained from ^{29}Si NMR
[c]Obtained from ^{27}Al NMR

Q^4(1Al), Q^3(0Al) and Q^4(3Al) [36,40,55]. After SCW treatment, the impure peaks in the range of −87 to −100 ppm, which were attributed to different acid sites, disappeared as well as −102 ppm, and the new peak at −91 ppm was observed corresponding to the framework Al in Si(1Si, 3Al). The peak strength around −106 ppm also markedly decreased. These results indicated the decrease of acid, Al and Si content in SCW-treated ZSM-5 was consistent with the NH_3-TPD profiles (Fig. 3). The reduction of peak strength at −112 ppm was also remarkable, attributed to the decrease of Si content in Si(4Si, 0Al) related to the obvious desilication in SCW-treated ZSM-5. As shown in Table 4, the framework Si/Al ratio increased from 19.1 to 30.3, and the relative intensity of Si(4Si, 0Al) increased from 78.7% to 92.9%. After SCW treatment, the unobvious peak of Q^3(0Al) indicated an increase of Q^4(0Al)/Q^3(0Al), and was accompanied by the increase of zeolite crystal size [40], which was consistent with the agglomeration of zeolites and the increase of d_{BET} according to XRD and BET data. The dealumination and the desilication of ZSM-5 were simultaneous in SCW, but the dealumination was more serious. The results also could be observed from FTIR data (Fig. 4).

The ^{27}Al NMR MAS spectra of parent and SCW-treated ZSM-5 are depicted in Fig. 5. The spectrum of parent ZSM-5 was dominated by a signal at 56.6 ppm assigned to tetrahedral coordinated framework Al [40,57]. A weaker signal at 1.2 ppm related to octahedrally coordinated extra-framework Al [57]. The relative intensity of tetrahedral (framework) and octahedral (extra-framework) Al in ZSM-5 before and after SCW treatment are shown in Table 4. 78.1% of tetrahedral Al decreased to 21.9%, but 28.9% of octahedral Al increased to 71.1%, due to the formation of a considerable amount of extra-framework by leaching framework Al from the zeolite lattice, which corresponded to the generation of strong or weak Lewis acid sites obtained from the NH_3-TPD result. The appearance of a new signal around 33 ppm signified a deformed tetrahedral framework Al or a penta-coordinated Al [57] and could be a transition state between tetrahedral Al and coordinated Al in SCW. The ^{27}Al NMR MAS spectra also showed the dealumination. Generally speaking, desilication of zeolite framework was because hydroxide ions attack Si-O-Si bonds in the zeolite framework, often occurring in hot liquid water, as shown in Eq. (1) [58]. Dealumination was attributed to hydronium ions attacking Si-O-Al bonds, often occurring in steam environment, as shown in Eq. (2) [58].

$$\equiv Si-O-Si\equiv + H-OH \leftrightarrow \equiv Si-OH + OH-Si\equiv \quad (1)$$

$$\equiv Al^- - O-Si\equiv + H-OH \leftrightarrow OH-Si\equiv + OH^- + Al \quad (2)$$

Both of the two degradation mechanisms existed during SCW treatment process, due to the state of SCW between liquid and steam. The attack rate of ions to framework bonds was quick in SCW and thus resulted in the serious collapse of crystalline structures in the zeolites.

CONCLUSIONS

The hydrothermal stability of zeolites in Supercritical water (SCW) mainly depended on their framework type, Si/Al, constituent elements in this study. The collapse of crystalline structure in 13X, HY, Beta, SAPO-11 and SAPO-34 was more serious than ZSM zeolites (TS-1 (titanium silicalite), ZSM-5 and ZSM-35). The crystalline structures of HY, Beta, SAPO-11 and SAPO-34 completely collapsed. The increase of relative crystallinity in 13X, TS-1, ZSM-5 and ZSM-35 was attributed to the increase of particle sizes due to the zeolite agglomeration. With the same framework type, 13X had higher hydrothermal stability than HY because the existence of extra-framework Al (EFAL) formed by leaching framework work could protect the framework against hydrolysis. Micropore surface areas of all zeolites decreased, but external surface area of 13X and ZSM zeolites increased. BET surface areas also decreased, except for TS-1 with the decrease of micropore surface area, the increase of external surface area and almost invariable BET surface area. TS-1 had the highest hydrothermal stability in the zeolites. Therefore, Titanium silicalite zeolite was more stable than aluminosilicate and silicoaluminophosphate zeolites.

After SCW treatment, the acid content of ZSM-5, TS-1, ZSM-35 and 13X was greatly reduced. SCW-treated zeolites generated strong Lewis acid sites due to the formation of EFAL, which the micropore structure remained in the zeolites. Desilication was simultaneous with dealumination in SCW, but dealumination was more serious. This phenomenon resulted in the increase of framework Si/Al ratio and the decrease of total acid content. During

SCW treatment process, tetrahedral (Framework) Al was transformed to deformed tetrahedral framework Al or penta-coordinated Al, and then octahedral (extra-framework) Al. According to the obtained results, some theoretical basis can be provided for making supported catalysts using supercritical water impregnation. In addition, SCW treatment can modify and regenerate zeolites to produce new zeolites or materials.

ACKNOWLEDGEMENTS

The authors are grateful for financial support from the National Natural Science Foundation of China (21277064), the Key Project of the Chinese Ministry of Education (210202), and the Analysis and Testing Foundation of Kunming University of Science and Technology (2017P2014607008).

SUPPORTING INFORMATION

Additional information as noted in the text. This information is available via the Internet at http://www.springer.com/chemistry/journal/11814.

REFERENCES

1. K. Sue, K. Murata, K. Kimura and K. Arai, *Green Chem.*, **5**, 659 (2003).
2. K. Sue, M. Suzuki, K. Arai, T. Ohashi, H. Ura, K. Matsui, Y. Hakuta, H. Hayashi, M. Watanabe and T. Hiaki, *Green Chem.*, **8**, 634 (2006).
3. T. Adschiri, Y. W. Lee, M. Goto and S. Takami, *Green Chem.*, **13**, 1380 (2011).
4. A. Aimable, H. Muhr, C. Gentric, F. Bernard, F. L. Cras and D. Aymes, *Powder Technol.*, **190**, 99 (2009).
5. J. W. Lee, J. H. Lee, T. T. Viet, J. Y. Lee, J. S. Kim and C. H. Lee, *Electrochim. Acta*, **55**, 3051 (2010).
6. D. Rangappa, T. Naka, S. Ohara and T. Adschiri, *Cryst. Growth Des.*, **10**, 11 (2010).
7. H. Li, T. Arita, S. Takami and T. Adschiri, *Prog. Cryst. Growth Ch.*, **57**, 117 (2011).
8. M. Hosseinpour, H. Amiri, S. J. Ahmadi and M. A. Mousavian, *J. Supercrit. Fluids*, **107**, 479 (2016).
9. K. J. Ziegler, R. C. Doty, K. P. Johnston and B. A. Korgel, *J. Am. Chem. Soc.*, **123**, 7797 (2001).
10. J. Otsu and Y. Oshima, *J. Supercrit. Fluids*, **33**, 61 (2005).
11. O. Sawai and Y. Oshima, *J. Supercrit. Fluids*, **47**, 240 (2008).
12. O. Sawai and Y. Oshima, *J. Mater. Sci.*, **43**, 2293 (2008).
13. D. Zhao, E. Han, X. Wu and H. Guan, *Mater. Lett.*, **60**, 3544 (2006).
14. C. B. Xu and A. S. Teja, *J. Supercrit. Fluids*, **39**, 135 (2006).
15. B. Qiu, L. N. Han, J. C. Wang, L. P. Chang and W. R. Bao, *Energy Fuel*, **25**, 591 (2011).
16. J. C. Wang, B. Qiu, L. N. Han, G. Feng, Y. F. Hu, L. P. Chang and W. R. Bao, *J. Hazard. Mater.*, **213**, 184 (2012).
17. K. S. Lin, H. P. Wang and Y. W. Yang, *Chemosphere*, **39**, 1385 (1999).
18. K. S. Lin and H. P. Wang, *Langmuir*, **16**, 2627 (2000).
19. K. S. Lin and H. P. Wang, *Appl. Catal. B-Environ.*, **22**, 261 (1999).
20. N. Mo, W. Tandar and P. E. Savage, *J. Supercrit. Fluids*, **102**, 73 (2015).
21. P. G. Duan, Y. P. Xu, F. Wang, B. Wang and W. H. Yan, *Biochem. Eng. J.*, **116**, 105 (2016).
22. K. Tomita, S. Koda and Y. Oshima, *Ind. Eng. Chem. Res.*, **41**, 3341 (2002).
23. Y. J. Lu, Y. M. Zhu, S. Li, X. M. Zhang and L. J. Guo, *Biomass Bioenergy*, **67**, 125 (2014).
24. Y. Karakuş, F. Aynacı, E. Kıpçak and M. Akgün, *Int. J. Hydrogen Energy*, **38**, 7298 (2013).
25. M. Akizuki and Y. Oshima, *J. Supercrit. Fluids*, **84**, 36 (2013).
26. N. Kometani, S. Hirata and M. Chikada, *J. Supercrit. Fluids*, **120**, 443 (2017).
27. A. Ashraf, S. A. Dastgheib, G. Mensing and M. A. Shannon, *J. Supercrit. Fluids*, **76**, 32 (2013).
28. Y. Matsumura, X. Xu and M. J. A. Jr., *Carbon*, **35**, 819 (1997).
29. F. Salvador, N. M. Sanchez, M. J. S. Montero, J. Montero and C. Lzquierdo, *J. Supercrit. Fluids*, **74**, 1 (2013).
30. G. Beaucage, H. K. Kammler and S. E. Pratsinis, *J. Appl. Crystallogr.*, **37**, 523 (2004).
31. T. Li, J. Cheng, R. Huang, W. J. Yang, J. H. Zhou and K. F. Cen, *Int. J. Hydrogen Energy*, **41**, 21883 (2016).
32. D. P. Serrano, G. Calleja, J. A. Botas and F. J. Gutierrez, *Sep. Purif. Technol.*, **54**, 1 (2007).
33. Y. Liu, W. P. Zhang, S. J. Xie, L. Y. Xu, X. W. Han and X. H. Bao, *J. Phys. Chem. B*, **112**, 1226 (2008).
34. M. B. Abda, O. Schäf, F. Ziarelli, H. Pizzala, R. Denoyel, S. Viel and Y. Zerega, *Micropor. Mesopor. Mater.*, **234**, 200 (2016).
35. S. Kumar, A. K. Sinha, S. G. Hegde and S. Sivasanker, *J. Mol. Catal. A-Chem.*, **154**, 115 (2000).
36. A. K. Jamil, O. Muraza, R. Osuga, E. N. Shafei, K. H. Choi, Z. H. Yamani, A. Somali and T. Yokoi, *J. Phys. Chem. C*, **120**, 22918 (2016).
37. W. Lutz, R. Kurzhals, S. Sauerbeck, H. Toufar, J. C. Buhl, T. Gesing, W. Altenburg and C. Jäger, *Micropor. Mesopor. Mater.*, **132**, 31 (2010).
38. L. H. Ding, Y. Zheng, Y. Hong and Z. Ring, *Micropor. Mesopor. Mater.*, **101**, 432 (2007).
39. R. M. Ravenelle, F. Schüβler, A. D. Amico, N. Danilina, J. A. V. Bokhoven, J. A. Lercher, C. W. Jones and C. Sievers, *J. Phys. Chem. C*, **114**, 19582 (2010).
40. J. Wang, J. C. Groen, W. B. Yue, W. Z. Zhou and M. O. Coppens, *J. Mater. Chem.*, **18**, 468 (2008).
41. K. S. W. Sing, D. H. Everett, R. A. W. Haul, L. Moscou, R. A. Pierotti, J. Rouquérol and T. Siemieniewska, *Pure Appl. Chem.*, **57**, 603 (1985).
42. A. M. Puziy, O. I. Poddubnaya, A. M. Alonso, A. C. Muñiz, F. S. García and J. M. D. Tascón, *Carbon*, **45**, 1941 (2007).
43. L. K. G. Bhatta, S. Subramanyam, M. D. Chengala, U. M. Bhatta and K. Venkatesh, *Ind. Eng. Chem. Res.*, **54**, 10876 (2015).
44. J. Aguado, D. P. Serrano, J. M. Escola and A. Peral, *J. Anal. Appl. Pyrol.*, **85**, 352 (2009).
45. D. P. Serrano, J. Aguado, J. M. Rodríguez and A. Peral, *J. Anal. Appl. Pyrol.*, **79**, 456 (2007).
46. E. Dumitriu, V. Hulea, I. Fechete, A. Auroux, J. F. Lacaze and C. Guimon, *Micropor. Mesopor. Mater.*, **43**, 341 (2001).
47. F. Lónyi and J. Valyon, *Thermochim. Acta*, **373**, 53 (2001).

48. F. Lónyi and J. Valyon, *Micropor. Mesopor. Mater.*, **47**, 293 (2001).
49. F. Frusteri, G. Bonura, C. Cannilla, G. D. Ferrante, A. Aloise, E. Catizzone, M. Migliori and G. Giordano, *Appl. Catal. B-Environ.*, **176**, 522 (2015).
50. M. A. Ali, B. Brisdon and W. J. Thomas, *Appl. Catal. A-Gen.*, **252**, 149 (2003).
51. P. Wang, B. J. Shen and J. S. Gao, *Catal. Today*, **125**, 155 (2007).
52. M. P. Moisés, P. P. D. Almeida, C. T. P. D. Silva, A. W. Rinaldi, E. M. Girotto, J. G. Meneguin, P. A. Arroyo, R. E. Bazan, S. L. Fávaro and E. Radovanovic, *RSC Adv.*, **4**, 48576 (2014).
53. K. V. V. S. B. S. R. Murthy, S. J. Kulkarni, M. Chandrakala, K. V. V. K. Mohan, P. Pal and T. S. R. P. Rao, *J. Porous Mater.*, **17**, 185 (2010).
54. D. R. C. Huybrechts, P. L. Buskens and P. A. Jacobs, *J. Mol. Catal.*, **71**, 129 (1992).
55. K. F. Lin, Z. H. Sun, S. Lin, D. Z. Jiang and F. S. Xiao, *Micropor. Mesopor. Mater.*, **72**, 193 (2004).
56. J. Datka, W. Kolidziejski, J. Klinowski and B. Sulikowski, *Catal. Lett.*, **19**, 159 (1993).
57. I. Hannus, Z. Kónya, J. B. Nagy, P. Lentz and I. Kiricsi, *Appl. Catal. B-Environ.*, **17**, 157 (1998).
58. W. Lutz, W. Gessner, R. Bertram, I. Pitsch and R. Fricke, *Micropor. Mater.*, **12**, 131 (1997).

Supporting Information

Hydrothermal stability of different zeolites in supercritical water: Implication for synthesis of supported catalysts by supercritical water impregnation

Yuechao Zhang, Yingjie Li, Junjie Gu, Senlin Tian†, and Ping Ning

Faculty of Environmental Science and Engineering, Kunming University of Science and Technology, Kunming, Yunnan 650500, China

(*Received 5 March 2018 • accepted 11 May 2018*)

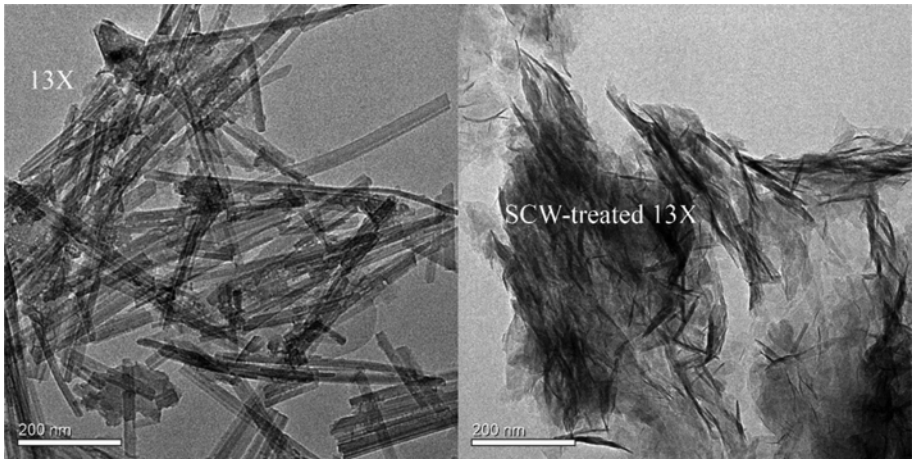

Fig. S1. TEM images of parent and SCW-treated 13X at 22.5 MPa, 385 °C and 10 min.

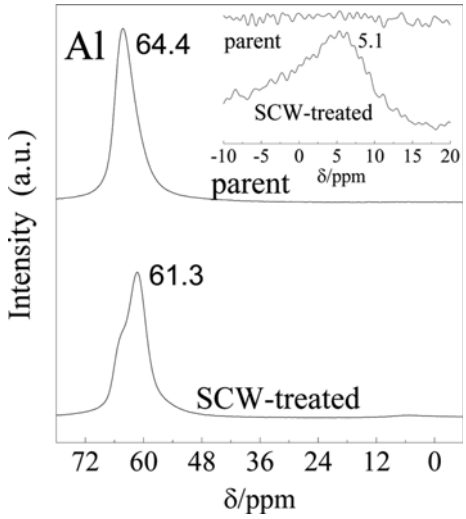

Fig. S2. ^{27}Al MAS NMR spectra of parent and SCW-treated 13X at 22.5 MPa, 385 °C and 10 min.

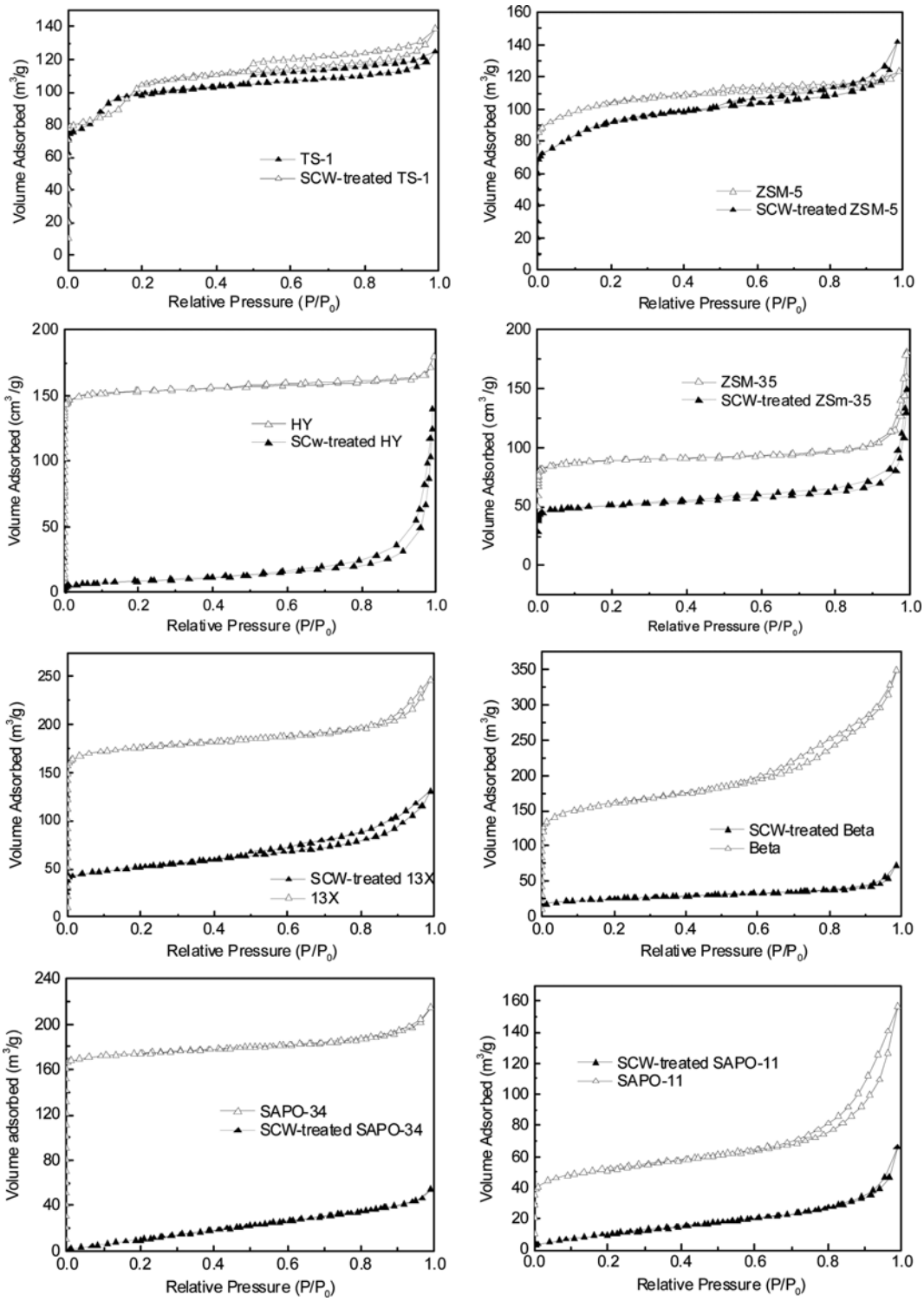

Fig. S3. Adsorption/desorption isotherms of N_2 at 77 K for before and after SCW treatment at 22.5 MPa, 385 °C and 10 min.

Table S1. Texture characteristics of parent zeolites and zeolites treated by SCW at 22.5 MPa, 385 °C and 10 min

		BET surface area (m^2/g)	Micropore surface area (m^2/g)	External surface area (m^2/g)	Average pore width (nm)	Average particle size (nm)	Total pore volume (m^3/g)	Micropore volume (m^3/g)
Parent	ZSM-5	365	320	45	2.09	16.44	0.193	0.143
	TS-1	363	321	42	2.12	16.52	0.197	0.136
	ZSM-35	322	300	22	3.22	15.87	0.262	0.127
	13X	615	551	64	2.48	9.75	0.378	0.246
	HY	631	611	20	1.73	11.54	0.273	0.230
	Beta	565	406	159	3.80	10.61	0.535	0.180
	SAPO-34	607	567	40	2.18	9.89	0.329	0.253
	SAPO-11	183	122	61	5.27	32.67	0.246	0.055
SCW-treated	ZSM-5	328	264	64	2.67	18.31	0.221	0.117
	TS-1	362	305	57	2.38	16.59	0.215	0.139
	ZSM-35	194	162	32	4.53	26.31	0.216	0.068
	13X	177	87	90	4.58	33.92	0.197	0.041
	HY	59	29	30	26.71	70.66	0.202	0.004
	Beta	91	53	38	4.93	65.66	0.110	0.024
	SAPO-34	55		55	6.06	108.90	0.085	
	SAPO-11	44		44	9.13	137.51	0.104	